Dalton Transactions

PAPER

Key role of higher order symmetry and electrostatic ligand field design in the magnetic relaxation of low-coordinate Er(III) complexes†

Saurabh Kumar Singh,[a,b] Bhawana Pandey, [iD][a] Gunasekaran Velmurugan[a] and Gopalan Rajaraman [iD] *[a]

The conceptual framework of electrostatic ligand field modulation based on oblate/prolate type electron density of lanthanide ions is one of the most successful approaches to enhance barrier height in lanthanide-based single-ion magnets. Recently, a tetra coordinated $[Er\{N(SiMe_3)_2\}_3Cl]\cdot 2THF$ (**1**) complex with an unfavourable ligand field showed slow relaxation of magnetization in zero field and challenges the concept of electrostatic ligand field modulation. To unravel the magnetic relaxation in this complex, we carried out a detailed theoretical investigation on three Er(III) complexes belonging to the same family of single-ion magnets. The CASSCF/PT2 + RASSI-SO approach highlights that the concept of electrostatic ligand field modulation based on oblate/prolate type is still valid in these complexes, and the relaxation dynamics observed can be rationalized by accounting for both the symmetry and geometrical distortions around the Er(III) ion. Using *ab initio* computed blockade barriers and crystal field analysis, we analysed the key components of the magnetic relaxation. Our study suggests that in these structures, the Er(III) ion shifted out of the triangular plane formed by the three nitrogen donor atoms and this out-of-plane shift (τ) significantly influences the slow-relaxation of magnetization. In order to gain deeper insights into the nature of metal–ligand bonding, and to predict quantitatively the strength of the axial and equatorial ligand field, ELF, QTAIM, and EDA analysis were carried out in these complexes. Our findings highlight that the molecules possessing large barrier height for magnetic relaxation are due to the combined effect of a favourable ligand field and the symmetry around the Er(III) ion. To understand the intricate role of both effects, several robust magneto-structural correlations were developed. Besides, the lanthanide-halogen covalency was also found to play a vital role in controlling the magnetic anisotropy and thus the magnetic relaxation. A near linear trend was observed between the calculated barrier height and the increase in the Er–X covalency as we move from –F to –I. This offers a *de novo* approach to increase barrier height in mononuclear lanthanide based complexes.

[a]Department of Chemistry, Indian Institute of Technology Bombay, Powai, Mumbai-400076, India. E-mail: rajaraman@chem.iitb.ac.in; Tel: +91-22-25767183
[b]Department of Molecular Theory and Spectroscopy, Max-Planck-Institute for Chemical Energy Conversion, Stiftstr.34-36, D-45470-Muelheim an der Ruhr, Germany
†Electronic supplementary information (ESI) available. See DOI: 10.1039/c6dt03568j

Introduction

Since the first observation of single-molecule magnet (SMM) characteristics in a monometallic {TbPc₂} complex[1] with a barrier height (U_{eff}) of 230 cm⁻¹, the study of lanthanide(III) ions has witnessed a rapid growth in producing high blocking temperature (T_B) SMMs.[2–9] Several potential applications ranging from magnetic information devices, *q*-bits in quantum computing to spintronic devices are proposed for these molecules.[10–15] Concrete efforts to enhance the U_{eff} value of lanthanide SMMs witnessed the report of very large U_{eff} values such as 652 cm⁻¹ observed for a derivative of {TbPc₂},[16] 585 cm⁻¹ for a polymetallic Dy@{Y₄K₂}[9] and 560 cm⁻¹ for {Ln(BIPM)₂} complexes.[17] Despite these impressive numbers, the observed blocking temperatures are always an order of magnitude smaller[4–6,8,18,19] and have been raised to as much as 60 K in recent years.[20]

Across the lanthanide series, Tb(III), Dy(III), and Er(III) are the most prolific ions towards the isolation of SMMs with rich magnetic properties.[2] This is essentially due to strong spin–orbit coupling effects in the ground LS terms. Recent discoveries suggest that enhancement of f-electron anisotropy lies at the heart of ligand field design based on the nature of the electron cloud (prolate/oblate) of lanthanide ions.[3] This strategy

led to the isolation of several new Ln(III) based SMMs (even based on lanthanides such as Ce, Nd, Yb, and Ho possessing lower magnetic moments).[21] A major problem associated with lanthanide based SMMs is the presence of quantum tunnelling of magnetization (QTM) effects, which offers a shortcut and drastically reduces the barrier height/T_B values.[2] In mononuclear lanthanide(III) ions, QTM can be diminished by attaining higher order local symmetry around the metal ion.[22] This is supported by the fact that most of the prominent SMMs preserve high order local symmetries such as D_{4d} (square antiprismatic structures), $D_{\infty h}$, (linear 2-coordinated), D_{3h} (for tri coordinated), and large rotational symmetry as observed in organometallic lanthanide complexes.[6,8,23–28]

Recent experimental and theoretical observations suggest that the presence of symmetry and stronger ligand field offers a viable way to enhance the U_{eff} values and quench QTM effects.[8,9,21,29–32,33–38] The role of higher order symmetry in conjunction with variation in coordination number in governing the relaxation pathways has been highlighted.[30] Low-coordinate complexes with the desired ligand field and higher order symmetry now are prime targets to achieve large U_{eff} values.[4–6,8,39–42]

In stark contrast to these concepts, [Li(THF)$_4$][Er{N (SiMe$_3$)$_2$}$_3$Cl]·2THF (**1**) mononuclear complex has been reported as a SMM with the U_{eff} value of 63.3 K (T_B ∼3 K).[43] This complex possess a negatively charged chloride ion in the axial position which is unfavourable for a prolate type Er(III) ion, yet noteworthy SMM characteristics are observed.[43] This opens up a new challenge to the existing concept of ligand field design based on the nature of electron cloud (prolate/ oblate). To understand the SMM characteristic observed in complex **1** and to check the robustness of existing concepts, here we have undertaken detailed CASSCF/RASSI-SO/ SINGLE_ANISO calculations. Our aim is to establish a clear road map between the symmetry and the ligand field strength, which can offer a way to design and rationalise the magnetic properties of such complexes.

Computational details

All *ab initio* calculations were performed using MOLCAS 8.0 suite.[44] We employed basis sets from the ANO-RCC library. As the basis sets strongly influence the magnetic anisotropy, here we performed calculations using two different basis sets. In the first set of basis set (named as BS1), we have employed: Cl ANO-RCC – 4s3p1d.; C ANO-RCC – 3s2p.; H ANO-RCC – 2s.; N ANORCC – 3s2p1d.; Si ANO-RCC – 4s3p1d.; Er ANO-RCC – 8s7p5d3f2g1h. For BS2 (higher level), the following basis sets were employed: Cl ANO-RCC – 5s4p2d.; C ANO-RCC – 3s2p1d.; H ANO-RCC – 2s1p.; N ANO-RCC – 4s3p2d.; Si ANO-RCC – 5s4p2d.; Er ANO-RCC – 9s8p6d4f3g2h. The ground-state f-electron configuration for Er(III) is 4f^{11} and this yields a $^4I_{15/2}$ multiplet as the ground state. First, we performed CASSCF calculations with an active space of 11 electrons in seven 4f orbitals (11,7). With this active space, we then computed 35 quartets as well

112 doublet states using the Configuration Interaction (CI) procedure. After computing these spin-free excited states, we mixed all these states using the RASSI-SO module to compute the spin–orbit states. In the next step, we used these computed spin–orbit states in the SINGLE_ANISO program to compute the g-tensors. Using the SINGLE_ANISO module, we computed g-tensor associated with eight low-lying KDs. For all the three complexes **1–3**, calculations were performed on crystallographic geometries. To observe the effect of charges (*i.e.*, neighbouring molecules in the lattice) on the electronic structure, we modelled the Madelung fields by incorporating four layers of point charges. Cholesky decomposition for two-electron integrals was employed throughout to save disk space. Using the SINGLE_ANISO code, we computed the CF parameters and constructed the *ab initio* blockade barrier[45] by computing the transversal magnetic moment between each KDs to analyse the nature of magnetic relaxation. To check the importance of dynamic correlation on the low-lying energy spectrum and associated magnetic anisotropy, N-electron valence second order perturbation theory (NEVPT2) calculations[46,47] were performed on complexes **1** and other halide analogues. All these NEVPT2 calculations were carried out in the ORCA suite of the software.[48] Here, we have used SARC basis set[49] for the Er(III) and def2-TZVP basis set[50,51] for the Cl, N, and Si atoms, and the def2-SVP basis set[50,51] for C and H. The low-lying energy spectrum for all –X analogues are provided in the ESI.†

DFT calculations were carried out using the Gaussian 09 suite to analyse spin-density and electrostatic potential maps.[52] Here we employed the B3LYP level of theory[53] with a Cundari–Stevens double zeta basis set[54] for Er(III) along with a TZV basis set[55] for the rest of the atoms. QTAIM analysis was carried out using the AIM2000 package.[56] Wave functions for use in QTAIM were generated from single point calculation using Gaussian 09. The ELF topological analysis was performed using Multi-wfn code.[57] In addition, the nature of the interactions between Er and Cl and (NSiMe)$_3$ ligands was analyzed using energy decomposition analysis, implemented in the ADF[58] program package based on the methods of Morokuma[59] and Ziegler[60] at the level of B3LYP/TZ2P with ZORA. The instantaneous interaction energy between the two fragments was calculated using the following equation:

$$\Delta E_{int} = \Delta E_{elstat} + \Delta E_{pauli} + \Delta E_{orb} \tag{1}$$

Results and discussion

Continuous symmetry shape measurement (CShM)[61] reveals that the coordination environment around the Er(III) ion in complex **1** is a distorted tetrahedral geometry with relatively large Er–Cl distance of 2.52 Å compared to the average Er–N distance of 2.24 Å (see Tables S1 and S2 of ESI† for details). Besides, the Er(III) ion is found to be out of the triangular plane formed by the equatorial –N atoms (out-of-plane shift τ is ∼0.45 Å). *Ab initio* calculations were performed on X-ray

crystallographic geometries of complex (**1**) (includes solvent and counter ion) and $[Er\{N(SiMe_3)_2\}_3Cl]^-$ (**1a**, where solvent and counter ions are removed) to determine the g-tensors and relative energies of Kramers doublets (KD) in the $^4I_{15/2}$ ground state of Er(III) ion.

The computed low-lying energy spectra of complexes **1** and **1a** spanned a range of 364 and 340 cm^{-1}, respectively. The gap between the ground state KD and the first excited KD is found to be 35.7 cm^{-1} and 37.6 cm^{-1} for complex **1** and **1a**, respectively. The computed g-tensors for the ground state doublet in **1** (g_{zz} = 17.8058, g_{yy} = 0.0226, and g_{xx} = 0.0165) and **1a** (g_{zz} = 17.8040, g_{yy} = 0.0229, and g_{xx} = 0.0181) are strongly axial but lack pure Ising type feature ($g_{xx} = g_{yy} = 0$). Explicit calculations on both **1** and **1a** clearly suggest that incorporation of counter-ion and solvent molecules does not influence the low-lying energy spectrum or the associated g-tensors (see Table 1). Henceforth, for simplicity, here onwards all the discussion will be restricted to complex **1a**.

In complex **1a**, the principal magnetization axis (g_{zz}) of the ground state KD is oriented towards the pseudo C_3 axis passing through the Er–Cl bond (see Fig. 1, Fig. S1 and S2 in ESI†).[62] The consequence of a higher degree of rotational symmetry in complex **1a** is clearly reflected in the orientation of the g_{zz} axis of the first three excited KDs, where they are found to be nearly collinear with that of the ground state g_{zz} axis (>$ca.$ 7 degree).[29,63] This implies that the major relaxation is expected to occur via the fourth excited state which is ~165 cm^{-1} higher in energy from the ground state KD ($vide$ $infra$). Moreover, the strong axial nature of the ground state KD is also confirmed from the very large negative B_2^0 term suggesting stabilisation of $|\pm15/2\rangle$ as the ground state. The presence of small but non-negligible B_2^q (where $q \neq 0$) terms reflect a deviation from the desired symmetry. Furthermore,
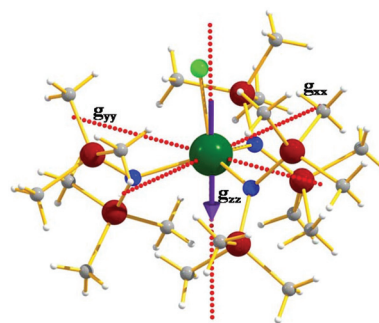

Fig. 1 Ab $initio$ computed g-tensor orientation of the ground state doublet. Color code: Er (green); N (blue); Si (dark red); C (brown); H (white).
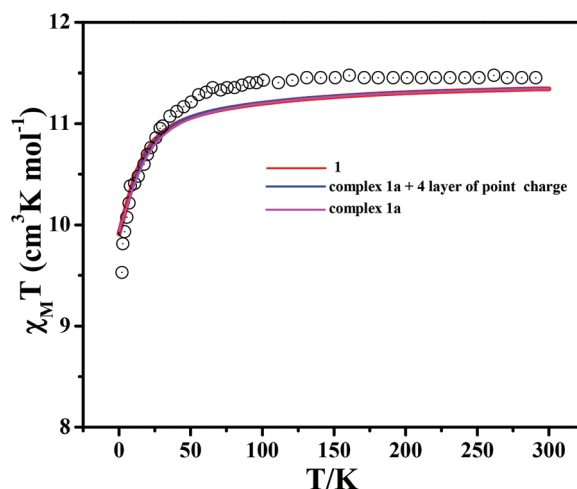

Fig. 2 Experimental and ab $initio$ computed molar magnetic susceptibility plots for complex **1**. The black hollow circle represents the experimental magnetic susceptibility extracted from the experimental data.[43] The coloured lines represent computed magnetic susceptibility.

calculations nicely reproduced the experimental magnetic susceptibility data, which adds confidence to our computed spin-Hamiltonian parameters (see Fig. 2 for details).

Mechanistic details of magnetic relaxation

To further understand the mechanism of magnetic relaxation, first we analysed the wavefunction of the ground state KD. The wavefunction decomposition analysis suggests that the ground state KD is predominantly $|\pm15/2\rangle$: $0.87|\pm15/2\rangle$ + $0.10|\pm9/2\rangle$ with a slight mixing from the excited $|\pm9/2\rangle$ state. This mixing arises due to presence of several low-lying excited states within ~100 cm^{-1} of energy window. The first three excited KDs are predominantly $|\pm13/2\rangle$, $|\pm11/2\rangle$, and $|\pm9/2\rangle$, however, the extent of mixing is significantly larger for these excited KDs (see Tables S3 and S4 of ESI†). The presence of several low-lying excited states might be due to weak Er–N interaction or a presence of unfavourable –Cl ligand on the axial position. To gain a better understanding of magnetic relaxation, we constructed the ab $initio$ blockade barrier by computing the transition
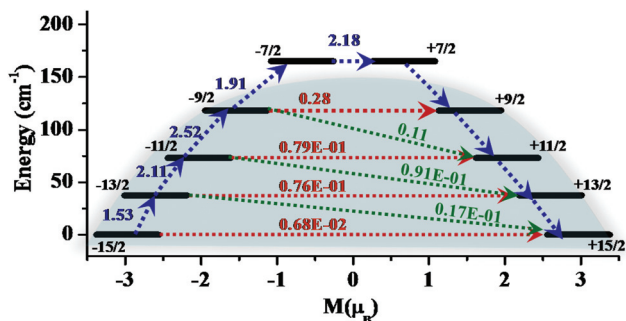
Table 1 CASSCF computed low-lying energies of eight KDs and associated g-tensors along with the deviation from the principal magnetization axes for complexes **1** and **1a**

J multiplets	Energies of KDs (cm^{-1})	g_{xx}	g_{yy}	g_{zz}	θ (°)
Complex 1a					
$^4I_{15/2}$	0.0	0.0181	0.0229	17.8040	—
	37.6	0.2132	0.2362	15.4317	3.3
	73.3	0.1142	0.3259	12.8153	3.3
	118.4	0.7399	0.8817	10.1359	7.6
	165.1	5.2421	6.0404	7.0070	93.4
	256.8	6.2791	6.1111	3.5832	5.5
	304.7	2.4546	3.7745	5.1933	58.9
	340.0	0.8895	5.0532	13.3627	87.2
Complex 1					
$^4I_{15/2}$	0.0	0.0165	0.0226	17.8058	—
	35.7	0.1692	0.1971	15.4928	6.3
	76.6	0.1497	0.2175	12.8619	6.4
	129.6	0.6648	0.6765	10.2087	6.0
	184.6	6.5582	6.0433	4.9189	99.0
	274.1	5.7386	5.4631	3.9823	9.4
	326.5	5.0046	3.9564	2.4955	35.8
	364.1	0.8947	5.0570	13.3671	85.2

Paper

Fig. 3 *Ab initio* blockade barrier for complex **1a**. The thick black lines indicate Kramer's doublets (KDs) as a function of magnetic moment. The green lines show the possible pathways of the Orbach process. The blue lines show the most probable relaxation pathways for magnetization reversal. The dotted red lines represent the presence of QTM/TA-QTM between the connecting pairs. The numbers provided on each arrow are the mean absolute values for the corresponding matrix elements of the transition magnetic moment. The labelled m_J states are not the pure eigenstates, but the most dominant ones; see text and ESI† for further details.

magnetic moments $((|\mu_X| + |\mu_Y| + |\mu_Z|)/3)$, between the connecting centres and these are displayed for complex **1a** (see Fig. 3).[45]

It is evident from Fig. 3, that the transition magnetic moment connecting the ground state $|\pm15/2\rangle$ is in the order of $\sim10^{-2}\mu_B$ (generally $\sim10^{-5}\mu_B$ is required for complete quenching of QTM effects).[30,45] Thus, presence of significant transition magnetic moment between ground state $|\pm15/2\rangle$ indicates a non-vanishing QTM in the ground state. However, the magnitude of the transition magnetic moments between other higher KDs, are larger by one or two orders of magnitude compared to the ground state KDs.

On the other hand, the largest moment of $2.18\mu_B$ is observed between the connecting $|\pm7/2\rangle$ state (fourth excited KD). The computed transition magnetic moment along with nearly collinear principal magnetisation axes suggests possible relaxation occurs *via* the 4th excited KD with an U_{cal} value of ~165 cm^{-1}.[24,29] However, a closer look at the *ab initio* blockade barrier indicates a strong thermally assisted QTM is operative *via* the 3rd excited KD as a $0.28\mu_B$ magnetic moment is detected between the $|\pm9/2\rangle$ KDs. Moreover, off-diagonal elements between the $|+9/2\rangle$ and $|-11/2\rangle$, which represent the Orbach relaxation, are also very significant ($0.11\mu_B$). Despite having near collinearity of principal magnetisation axes, the presence of these two strong relaxation pathways do not allow the blockade to reach up to the 4th excited KD. This is also affirmed by the significant drop in the transition magnetic moments of $|+9/2\rangle \rightarrow |+7/2\rangle$ state. Thus, the thermally-assisted magnetic relaxation is expected to occur *via* the 3rd excited state which places the U_{cal} value as 118 cm^{-1}. The calculated barrier height of 118 cm^{-1} is significantly large compared to the experimental barrier height of 44 cm^{-1}. From the *ab initio* computed blockade barrier, it is evident that several competing pathways are operational *via* ground and first/second excited states as a result of low-symmetry and an unfavourable

–Cl ligand in the axial position. Moreover, it is important to note here that the *ab initio* computed blockade barrier is a qualitative picture of the magnetic relaxation; however, in reality, intermolecular interactions and spin–phonon bath interactions also play a role in the magnetization relaxation. In our previous contribution, we found that intermolecular interactions open multiple pathways and suppress the barrier height of Er(III) SIM more than ten times, compared to diluted samples. A nice agreement in an earlier study was found between experimental results and the computed values, when parameters obtained from diluted samples were compared.[64] Besides, experimental data[43] clearly reveal presence of other relaxation processes, such as Raman, in a higher temperature regime.

In order to treat the effect of the lattice and surroundings on the computed low-lying spectrum and magnetic anisotropy, we employed the embedded cluster approach.[65] Here, first we grew the super cell ($4 \times 4 \times 4$) and divided this into two regions (see Fig. 4). The first zone is the quantum core where explicit CASSCF calculations are performed to compute the magnetic anisotropy. The second zone is considered as the point charges region to mimic intermolecular effects. Here, we have considered CASSCF computed charges as the point charge with the principle of charge neutrality ($q^{QC} = -q^{PC}$). The computed low-lying spectrum has maximal change of 10 percent with the U_{cal} value of ~141 cm^{-1} (ground state-third excited KDs gap). For the ground state KD, the computed g-tensors are ($g_{xx} = 0.0120$, $g_{yy} = 0.0156$, and $g_{zz} = 17.831$) strongly axial in nature. The computed properties with the embedded approach are very similar to those of naked complexes (**1** and **1a**, see Tables S5 and S6 in ESI†). This approach is very effective in mimicking solid-state effects; however, the molecule of our interest is rather discrete; thus, these effects are unlikely to change the computed properties of the individual molecule. The computed low-lying energy spectrum, associated g-tensors, and wavefunction decomposition analysis are shown in Tables S3 and S4 of ESI.† To check the influence of the
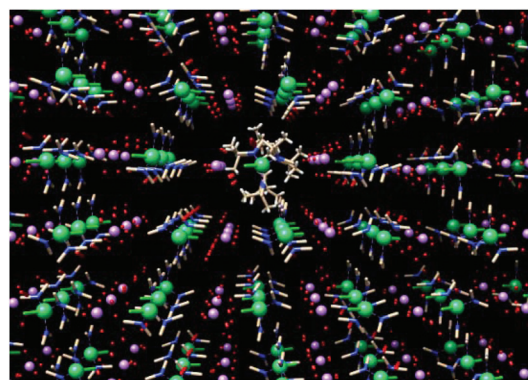
Fig. 4 $4 \times 4 \times 4$ super cell packing diagram for complex **1** used for embedding the cluster environment. Color code: green Er, red O, pink Li, and blue N. Quantum core in the centre is represented by a stick model.

basis set (from double zeta to triple zeta), additional calculations were performed using the triple zeta basis set (@BS2 level, see Table S7†) and the computed low-lying energy spectrum changed marginally by ~5–10 percent.[66] Thus, the discrepancy between the calculated and the experimental barrier height could be attributed to intermolecular interactions/significant QTM effects/hyperfine interactions/multi-phonon relaxation paths.[64] Quite interestingly, a magnetically diluted sample[43] of complex **1** ([$Er_{0.1}Y_{0.9}${$(Me_3Si)_2N$}$_3$(μ-Cl){Li-$(THF)_3$}] (**2**)) exhibited a smaller barrier height of 38.7 cm^{-1} which is contrary to general dilution effects observed in Er(III) SIMs.[6,64]

A closer look at the crystal structure reveals that complex **2** has larger distortion around Er(III) compared to complex **1** (see Tables S1 and S2 of ESI†). The presence of structural distortion led to a dramatic change in the magnetic relaxation pattern for complex **2**. Calculations disclose ~25 percent reduction in the energy spectrum of eight low-lying KDs, with the first excited KD being ~28 cm^{-1} higher in energy from the ground state (see Table S8 of ESI†). Calculations suggest that the major relaxation path for magnetic relaxation in complex **2** occurs via the first excited state as the g_{zz} axis of first excited state is 33° tilted compared to the ground state, leading to a very small barrier height. Therefore, the experimentally observed barrier for **2** cannot be directly compared to the calculated barrier of **1**.

To gain deeper insight into impact of the strength of the Er–Cl ligand on the low-lying spectrum and magnetic anisotropy of Er(III) ion, we developed a magneto-structural correlation by varying the Er–Cl bond distance from 2.4 Å to 3.2 Å, while keeping all other structural parameters intact. It is evident from Fig. 5 that an increase in the Er–Cl bond distance led to a near linear increase in the U_{cal} values.

The largest U_{cal} value is observed for the structure with an Er–Cl bond distance of 3.2 Å. The observed trend agrees with the ligand field paradigm proposed for the prolate type ion. We also plotted the evolution of all the eight low-lying KDs with respect to changes in the Er–Cl bond distance. From Fig. 5b, it is evident that relative energies of all the low-lying excited KDs increase linearly with increase in the Er–Cl bond distance and this highlights how sensitive the low-lying energy spectrum of the Er(III) ion is with respect to the strength of the Er–Cl interaction.
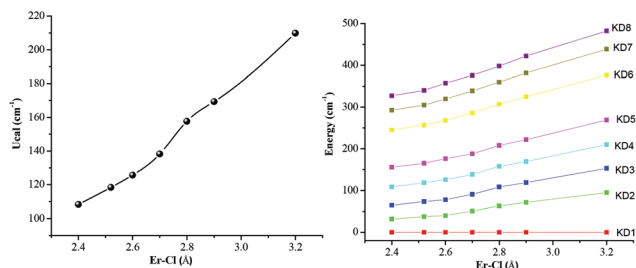
Fig. 5 (a) Magneto-structural correlation performed by varying Er–Cl bond distance in complex **1a**. CASSCF + RASSI computed U_{cal} values for each different structure (left); (b) *ab initio* computed energy levels as a function of Er–Cl bond distance (right). All these points emerged from the CASSCF + RASSI calculations on each structure.

The second and most noticeable feature is the gap between the ground and first excited state which changes drastically with change in the Er–Cl bond distance compared to other KDs. For the prolate type ions, $|\pm 15/2\rangle$ KD has the strongest repulsion from axial ligands; thus, elongation of the Er–Cl bond distance stabilizes $|\pm 15/2\rangle$ KD to a much larger extent compared to other excited KDs. This led to a larger ground state-excited state gap, which in principle diminishes the extent of admixing from the excited states and quenches the QTM process. It is obvious from the developed magneto-structural correlation that the complete extraction of the –Cl ion will lead to an ideal situation for the prolate type Er(III) ion with only three –N donors in the equatorial plane. Additional calculations were performed on the model complex [$Er(NSiMe_3)_3$] (**1m**) *i.e.*, complex **1a** without a –Cl ligand, and we observed a significant increase in the energy window of the low-lying energy spectrum, with a first excited state lying at ~161 cm^{-1} higher in energy from the ground state KD. As a result, the computed g-values (g_{zz} = 17.8767, g_{yy} = 0.0016, and g_{xx} = 0.0014) for the ground state KD in **1m** also reflect a higher degree of axiality compared to **1a** (see Table S9 of ESI†). For model **1m**, the relaxation occurs via the fifth excited KD with U_{cal} value 557.4 cm^{-1}.[29] The computed U_{cal} value for the model complex **1m** is nearly ~100 cm^{-1} larger than the value computed on the X-ray structure of [$Er(NSiMe_3)_3$] complex reported by Tang and co-workers.[24] A careful analysis of the structural parameters of complex **1m** and the [$Er(NSiMe_3)_3$] complex reported by Tang and co-workers[67] reveals a small but significant change in the out-of-plane shift parameter (τ, defines the pyramidalisation shift around the {ErN3} plane, with zero value denoting a totally planar molecule; see ref. 60 for further details). For complex **1m**, the out-of-plane shift (τ) parameter is found to be ~0.45 Å which is slightly smaller than 0.57 Å observed for the [$Er(NSiMe_3)_3$] complex.[67] In our previous contribution on the studies of magnetic anisotropy in tri-coordinate Er(III) complexes, we highlighted that an out-of-plane shift (τ) parameter is the key parameter which governs the magnetic relaxation in these classes of complexes.[29] Moreover, a robust magneto-structural correlation was established between the low-lying energy spectrum and out-of-plane shift (τ) parameter. The difference attributed in the computed barrier height can be nicely rationalized from our previously developed magneto-structural correlation.[24,29] The situation of complex **1a** can be better understood by the fact that the unfavourable axial ligand field offered by –Cl is partially compensated, as this pushes the Er(III) ion towards the triangular plane (lower τ value).[43] As a result, complex **1a** shows slow relaxation of magnetisation with a U_{eff} value of 44 cm^{-1} (T_B ~3 K). This has been further supported by a recent report where a similar complex with different counter-ion ([$Er(NSiMe_3)_3Cl$]$^{-}$ (**3**)) possessing an even smaller τ value (0.43 Å) apparently resulted in an improvised U_{eff} value of 49 cm^{-1} compared to complex **1**.[67] To crosscheck our predictions, additional calculations were performed on complex **3**, and the U_{cal} value was found to be 125 cm^{-1} which is slightly higher than that of complex **1a** (118 cm^{-1}). A nice trend has been
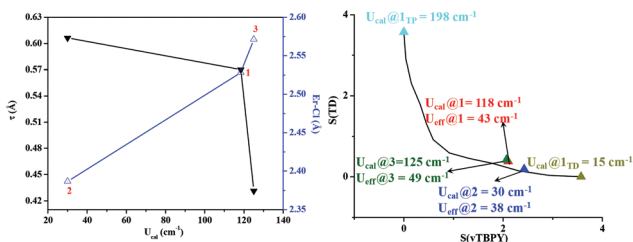
Fig. 6 (a) Two dimensional plot representing the dependency of U_{cal} value on the Er–Cl bond distance and τ parameter; (b) continuous symmetry map representing minimal distortion pathway between tetrahedral (TD,) and axially vacant trigonal bipyramid (vTBPY) for studied Er(III) complexes along with the mapped U_{eff} (experimental) U_{cal} values (calculated).

Fig. 7 *Ab initio* blockade barrier for model complex 1_{TD} (left; **7a**) and 1_{TP} (right; **7b**). The thick black lines indicate Kramer's doublets (KDs) as a function of magnetic moment. The green lines show the possible pathways of the Orbach process. The blue lines show the most probable relaxation pathways for magnetization reversal. The dotted red lines represent the presence of QTM/TA-QTM between the connecting pairs. The numbers provided on each arrow are the mean absolute values for the corresponding matrix elements of the transition magnetic moments.

observed between the U_{cal} *vs.* Er–Cl distance/τ parameter (see Fig. 6). This highlights that not only the ligand field environment around the Er(III) plays a key role in governing the magnetic anisotropy but also the local structural distortions.

Our detailed theoretical investigation nicely explains the experimental trend of the SMM performances of complexes **1–3**. Here, we would like to bring attention to complex **2**, the magnetically diluted sample of complex **1** which possess a relatively smaller barrier height for magnetic relaxation. A closer look into the crystal structure of complex **2** reveals that, the Er(III) ion possess a slightly different crystal structure. Complex **2** has a relatively large τ parameter ~0.61 Å and this is significantly larger than that of complex **1** (~0.45 Å) and **3** (~0.43 Å). The second noticeable difference is in the Er–Cl bond distance, which is found to be 2.38 Å, and this is significantly smaller compared to complex **1** (2.52 Å) and complex **3** (2.57 Å). However, we would like to note here that the nature of the Cl ion present in complex **2** is different compared to **1** and **3** because in complex **2** the Cl ion is bound strongly to the [Li(THF)$_3$]$^+$ cation and this Cl–Li bonding influences the Er–Cl distance. Thus, both the small Er–Cl bond distance and large τ parameter associated with complex **2** suggests that this is perhaps closer to the tetrahedral geometry (T_D, see below).

Influence of symmetry on the magnetic anisotropy

In the first two sections we discussed the nature of an axial ligand and local structural distortions such as out-of-plane shift (τ) parameters on the magnetic anisotropy of the Er(III) ion. Apart from ligand field strength, another parameter which strongly influences magnetic anisotropy is the symmetry around the Ln(III) ions. In this section, we have focussed our attention to understand the role of symmetry in building a highly anisotropic environment around the Er(III) ion. To address this issue, we performed CShM analysis using SHAPE software, which offers a way to quantify the degree of distortion on the coordination sphere of reported structures.[61] For coordination number four, initially, we generated two highly symmetric structures of complex **1a**; *i.e.*, perfect tetrahedral (1_{TD}) and trigonal pyramidal (1_{TP}) geometries. Calculations were carried out on both the symmetric structures to analyse the nature of *g*-tensors and the low-lying energy spectrum. For
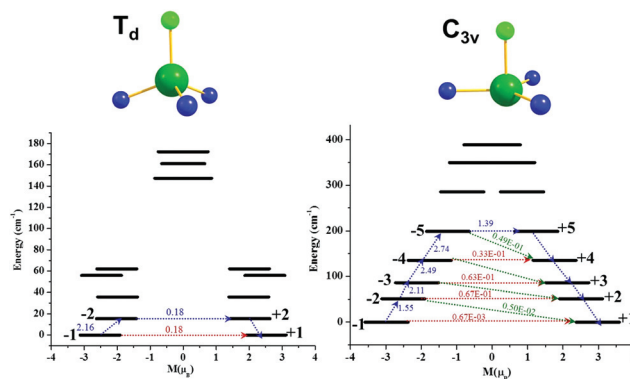
model complex 1_{TD}, the energy window of eight KDs falls in a narrow range of 172 cm^{-1} with a first excited state being just 15 cm^{-1} higher from the ground state. As compared to complex **1a**, the energy window of complex 1_{TD} is ~50 percent lower because of an unfavourable ligand field produced by tetrahedral geometry. The computed *g*-tensor for the ground state (g_{zz} = 15.09973, g_{yy} = 0.60099, and g_{xx} = 0.52102) has a significant transverse component, suggesting QTM to be dominant in this symmetry (see Fig. 7, Tables S10 and S11 in ESI†). On the other hand, for model complex 1_{TP} (τ ~0 Å) where all three –N atoms are in a plane of Er(III) ion, the first excited state is found to be located at ~51.4 cm^{-1} from the ground state KD with an energy window of eight KDs spanned over a range of ~389 cm^{-1}. The ground state *g*-value is found to be (g_{zz} = 17.87069, g_{yy} = 0.00217, and g_{xx} = 0.00189) strongly axial in nature compared to complex **1a**. Moreover, in complex 1_{TP}, we observed strict collinearity of the g_{zz} axes among all the excited KDs; however, matrix elements of the transition magnetic moment suggest relaxation *via* the 5th excited state with an estimated barrier height of 199 cm^{-1} (see Fig. 7).

We mapped the computed and experimental barrier height of all the studied complexes **1–3** along with two model complexes 1_{TD} and 1_{TP} on the minimal distortion pathway between the trigonal prismatic and tetrahedral geometry. It is evident from Fig. 6b that, as we move towards the trigonal pyramidal (C_{3v} symmetry) geometry, the barrier height increases in a near exponential manner. This correlation helps to rationalise the SMM behaviour for various tetra coordinated Er(III) molecules.

Furthermore, to check the robustness of the particular ligand environment for oblate type ions, additional calculations were performed on the [Dy{N(SiMe$_3$)$_2$}$_3$Cl]$^-$ complex. The calculated barrier height was found to be 54.2 cm^{-1} with significant transverse *g*-values for the ground state (g_{xx} = 0.66463, g_{yy} = 2.4727, g_{zz} = 17.5698, see Table S12 in ESI†). Thus, our study suggests that coordination number four with

trigonal pyramidal or tetrahedral geometry is not an ideal geometry either for oblate or prolate type ions for obtaining large magnetic anisotropy. At the same time, trigonal pyramidal geometry is relatively better than tetrahedral geometry for prolate type ions and *vice versa* for oblate type ions.

Ab initio crystal field analysis

To analyse the effect of symmetry on QTM, we cross-compared the crystal field (CF) parameters of $\mathbf{1a}$, $\mathbf{1_{TD}}$, and $\mathbf{1_{TP}}$. In the absence of intermolecular interactions and hyperfine interactions, the probability of QTM can be best described by crystal field parameters. The crystal field Hamiltonian is given by $\hat{H}_{CF} = B_k^q O_k^q$ where B_k^q is the crystal field operator while O_k^q is the Steven's operator. The computed crystal field parameters for complex $\mathbf{1a}$, $\mathbf{1_{TD}}$, and $\mathbf{1_{TP}}$ are listed in the Table 2. It is evident from Table 2 that the axial B_2^0 term is negative and the magnitude is large compared to other non-axial B_2^1, B_2^2 and B_4^2 terms. This indicates that the ligand field arrangement stabilises the largest $m_J = |\pm 15/2\rangle$, state for all three cases; however, the ratio of non-axial and the axial terms are governed by the corresponding point-group symmetry. The magnitude of the non-axial terms are almost two orders smaller than the axial term for complex $\mathbf{1_{TP}}$, while one order smaller for complex $\mathbf{1a}$ and almost equal for complex $\mathbf{1_{TD}}$. This is correlated to the SMM characteristics and yields the following order of decreasing U_{cal} values $\mathbf{1_{TP}} > \mathbf{1a} > \mathbf{1_{TD}}$.

This corroborates the magneto-structural correlation (see Fig. 6b), where the calculated barrier heights are mapped on a minimum distortion pathway between the two ideal geometries (see Fig. 6b and 7), where a large barrier height for the trigonal pyramidal structure and lower barrier height for tetrahedral geometry are observed. The computed CF parameter for complexes $\mathbf{1}$–$\mathbf{3}$ supports the trend of the SMM characteristic. Experimental observations of U_{eff} trend $\mathbf{3} > \mathbf{1} > \mathbf{2}$ can be explained by smaller τ values, longer Er–Cl distance, and the symmetry being closer to idealized trigonal-prismatic geometry.

Role of heavier halide ions in the nature of magnetic anisotropy

In the final section, we have attempted to understand the role of heavier halide ions on the nature of magnetic anisotropy of the Er(III) ion, as they are well known to influence metal–ligand covalency and apparently magnetic anisotropy.[68,69] This is well known in the field of transition metal chemistry; however, it has not been theoretically predicted/observed for lanthanide complexes. In stark contrast to the transition metal complexes, where covalency strongly influence magnetic and spectral properties, lanthanide–ligand covalency is expected not to influence the anisotropy significantly as 4f-shells are deeply buried. However, properties like magnetic exchange interactions in lanthanide complexes demand the presence of vacant 5d/6s orbitals,[70–74] and thus they play a crucial role in metal–ligand bonding. In order to analyse the effect of the heavier halide on the single-ion anisotropy of Er(III) ion, we considered three model complexes of $[Er\{N(SiMe_3)_2\}_3X]^-$ (X = F ($\mathbf{1\text{-}F}$), Br ($\mathbf{1\text{-}Br}$), I ($\mathbf{1\text{-}I}$)) where Er–X bond distances are maintained as observed in the literature.[75]

CASSCF + RASSI-SO calculations show remarkable changes in the low-lying spectrum of these model complexes compared to the parent complex $\mathbf{1a}$. The gap between the ground and first excited state has changed dramatically, from 37 cm^{-1} ($\mathbf{1a}$) to 16 cm^{-1}, 57 cm^{-1} and 75 cm^{-1} for –F, –Br and –I analogues, respectively (see Tables S13–S15 in ESI†).

Although the position of the –X ion is unfavourable, the presence of heavier halides offers larger contributions from the low-lying spin-free excited states leading to a highly anisotropic ground state. Besides, the QTM effects are decreased significantly, as we move from –F to –I (0.11μ_B for F, *vs.* 0.002μ_B for I). The barrier height is found to be ~16.0 cm^{-1}, ~146 cm^{-1} and ~178 cm^{-1} for –F, –Br and –I complexes, respectively. Quite interestingly, a linear relationship has been observed between the LoProp computed charges[76] on the –X ions *vs.* U_{cal} values indicating how lanthanide–ligand covalency alters the barrier height (see Fig. 8 and ESI† for details).

To check the influence of the dynamic correlation on the quantitative estimation of the spectroscopic terms[77] (splitting of J's), CASSCF/NEVPT2 calculations[48] were carried out on all the Er–X model complexes. The observations from the dynamic correlations are in accordance with the CASSCF results validating our results (see ESI Tables S16–S19† for details). In order to gain more insight into the nature of Er–X bond and to quantify the covalency, we analysed the reduced Löwdin orbital population analysis obtained from CASSCF densities (see Table S20 of ESI† for details). It is well known that the Er–X bonds are ionic in nature with a small covalency

Table 2 CASSCF + RASSI-SO computed crystal field parameters of Complex $\mathbf{1a}$ and $\mathbf{1_{TD}}$ and complex $\mathbf{1_{TP}}$

| k	q	Complex $\mathbf{1_{TD}}$ B_k^q	Complex $\mathbf{1a}$	Complex $\mathbf{1_{TP}}$ B_k^q
2	−2	-0.3824×10^{-1}	0.2548×10^{0}	0.4411×10^{-1}
	−1	$\mathbf{-0.1745 \times 10^{0}}$	-0.4451×10^{0}	0.5030×10^{-1}
	0	$\mathbf{-0.7160 \times 10^{0}}$	$\mathbf{-0.2025 \times 10^{1}}$	$\mathbf{-0.2203 \times 10^{1}}$
	1	$\mathbf{-0.2014 \times 10^{0}}$	-0.7480×10^{0}	0.8121×10^{-1}
	2	0.6079×10^{-1}	0.8028×10^{-1}	-0.1736×10^{-1}
4	−4	-0.3873×10^{-3}	0.1015×10^{-2}	0.1707×10^{-3}
	−3	$\mathbf{-0.4933 \times 10^{-1}}$	-0.5741×10^{-2}	$\mathbf{-0.1053 \times 10^{-1}}$
	−2	0.1986×10^{-2}	0.2361×10^{-2}	-0.1334×10^{-3}
	−1	0.1837×10^{-2}	0.2920×10^{-2}	-0.1737×10^{-3}
	0	0.1923×10^{-2}	0.2708×10^{-2}	0.3576×10^{-2}
	1	0.1978×10^{-2}	0.4812×10^{-2}	-0.6109×10^{-3}
	2	0.9369×10^{-3}	-0.1771×10^{-2}	-0.8056×10^{-4}
	3	$\mathbf{0.2008 \times 10^{-1}}$	$\mathbf{0.4772 \times 10^{-1}}$	$\mathbf{0.1923 \times 10^{-1}}$
	4	0.2003×10^{-2}	0.3092×10^{-3}	0.4027×10^{-4}
6	−6	$\mathbf{-0.2304 \times 10^{-3}}$	$\mathbf{0.2125 \times 10^{-3}}$	$\mathbf{0.2050 \times 10^{-3}}$
	−5	0.7574×10^{-4}	-0.1424×10^{-4}	0.3442×10^{-5}
	−4	0.5352×10^{-5}	-0.4003×10^{-4}	-0.1118×10^{-6}
	−3	$\mathbf{0.1935 \times 10^{-3}}$	-0.3595×10^{-4}	$\mathbf{0.1823 \times 10^{-3}}$
	−2	-0.2536×10^{-4}	-0.2798×10^{-4}	0.5418×10^{-5}
	−1	0.3046×10^{-4}	0.2628×10^{-5}	0.8128×10^{-5}
	0	0.1229×10^{-4}	-0.4135×10^{-5}	-0.1444×10^{-4}
	1	0.2595×10^{-4}	-0.3985×10^{-5}	0.3581×10^{-5}
	2	0.7152×10^{-6}	0.4374×10^{-4}	-0.1335×10^{-5}
	3	$\mathbf{-0.1822 \times 10^{-3}}$	$\mathbf{-0.3550 \times 10^{-3}}$	$\mathbf{-0.1447 \times 10^{-3}}$
	4	-0.2873×10^{-4}	-0.2761×10^{-4}	0.9672×10^{-5}
	5	0.6750×10^{-4}	-0.5276×10^{-4}	0.1234×10^{-4}
	6	0.2215×10^{-4}	0.5941×10^{-4}	0.2950×10^{-5}
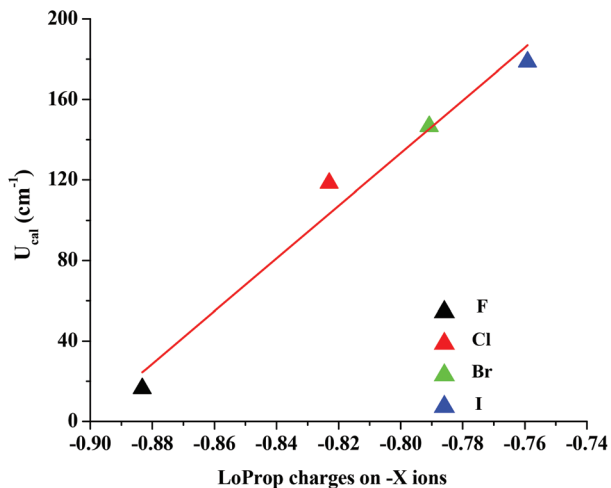
Fig. 8 The plot of observed U_{cal} values in $[Er\{N(SiMe_3)_2\}_3X]^-$ (where X = F, Cl, Br, and I) *vs.* LoProp charge on −X ions.

effect, while the latter term is expected to increase as we move towards the heavier halide. It is evident from population analysis that the vacant 5d/6s/6p orbitals of Er(III) ion along with the 4f ion gain significant population from the halide ion and this can be directly correlated to the lanthanide–ligand covalency. Interestingly, the populations of the vacant 5d orbital of the Er(III) ion in Er–X complexes are found to be (0.76)F, (0.93)Cl, (0.99)Br, and (1.08)I and this corroborates that Er–X covalency increases as we move down to the heavier halogens. Our calculations recommend utilizing heavier halides in the coordination sphere as this maximize the gap between the m_J states, and quench the QTM effects to a certain extent. It is important to note here that more rigorous and quantitative analysis of covalency and magnetic anisotropy demands the incorporation of these 5d, 6s, and 6p orbitals along with ligand orbitals in the active space which is currently a bottleneck for large molecules.

## Nature of bonding in complex 1

In this section, we will focus our attention to quantify the strength of the metal–ligand interaction, as this will help us to probe, how the electrostatic ligand field perturb the magnetic anisotropy of the Er(III) ion. In order to describe the role of the –Cl ligand and –N ligands on the magnetic properties of Er(III) ions, we analysed the donor strength of the ligands by means of QTAIM and ELF calculations.[78–80,81] The QTAIM analysis supports the Er–N and Er–X (X = F, Cl, Br and I) bond paths, as we have observed a bond critical point between the Er(III) cation and –N and –X ligands (see Fig. S3 in ESI†). QTAIM displays BCPs (bond critical point) representing the bonded and the non-bonded interactions that exist in complex **1a**. Importantly, the small values of electron density $(\rho(r))$ (<0.1 au), positive Laplacian $\nabla^2_{\rho(r)}$ (0.042–0.066 au) and negative values of total electronic energy density $H(r)$ ($H(r) = G(r) + V(r)$ where $G(r)$ and $V(r)$ are the local electron potential and kinetic energy density, respectively) at the BCP reflects the presence of closed shell interactions (electrostatic interaction).[82] This is supported by the values of the $|V(r)|/G(r)$ ratio. If this ratio is less than 1, then an interaction is ionic and if it is greater than 2 then the interaction is covalent in nature.

For complex **1a** (X = Cl), this ratio is estimated to be 1.18 and this suggests an electrostatic ligand field interaction with the Er(III) ion. A relatively large electron density observed for the Er–N bond compared to the Er–Cl bond suggests a stronger electrostatic repulsion from the equatorial ligand than the axial ligand (see Table 3) and rationalizes the reason for the observance of SMM behaviour in this complex. The calculated $\rho(r)$ values in Er⋯X (X = F, Cl, Br, and I) bonds are predicted in the range of 0.051–0.123 au, whereas the values of $\nabla^2_{\rho(r)}$ are all positive, ranging from 0.033–0.116 au. The $H(r)$ is also negative in all the cases. This suggests that the interaction between the Er(III) ion and halogen is electrostatic in nature. Fig. 9 shows the contour maps of the Laplacian of electron density $\nabla^2_{\rho(r)}$ along the Er–X (X = F, Cl, Br, and I).

Table 3 Topological parameters at BCPs in the Er−X and Er−N bonds of complex $[Er\{N(SiMe_3)_2\}_3X]^-$ (X = F, Cl, Br, and I). $\rho(r)$ in units of e Å^{-3}, $G(r)$, $V(r)$, and $H(r)$ in units of au

		$\rho(r)$	$\nabla^2_{\rho(r)}$	$H(r)$	$G(r)$	ε	$V(r)$	$|V(r)|/G(r)$
1-F	Er⋯F	0.096	0.116	−0.016	0.132	0.028	0.149	1.123
	Er⋯N1	0.076	0.065	−0.013	0.078	0.117	0.091	1.164
	Er⋯N2	0.074	0.065	−0.012	0.077	0.222	0.089	1.156
	Er⋯N3	0.073	0.066	−0.012	0.078	0.123	0.089	1.148
1a	Er⋯Cl	0.057	0.042	−0.009	0.051	0.012	0.060	1.180
	Er⋯N1	0.078	0.066	−0.014	0.080	0.097	0.094	1.173
	Er⋯N2	0.075	0.063	−0.013	0.076	0.140	0.089	1.167
	Er⋯N3	0.076	0.063	−0.013	0.076	0.133	0.089	1.171
1-Br	Er⋯Br	0.051	0.033	−0.007	0.040	0.014	0.047	1.187
	Er⋯N1	0.076	0.066	−0.013	0.080	0.161	0.093	1.163
	Er⋯N2	0.075	0.065	−0.013	0.078	0.154	0.091	1.160
	Er⋯N3	0.078	0.067	−0.014	0.081	0.088	0.094	1.172
1-I	Er⋯I	0.123	0.037	−0.094	0.130	0.200	0.224	1.172
	Er⋯N1	0.073	0.081	0.015	0.096	1.054	0.111	1.158
	Er⋯N2	0.074	0.083	−0.016	0.099	0.950	0.115	1.160
	Er⋯N3	0.075	0.083	−0.015	0.098	0.652	0.114	1.157

$[Er\{N(SiMe_3)_2\}_3F]^-$

$[Er\{N(SiMe_3)_2\}_3Cl]^-$

$[Er\{N(SiMe_3)_2\}_3Br]^-$
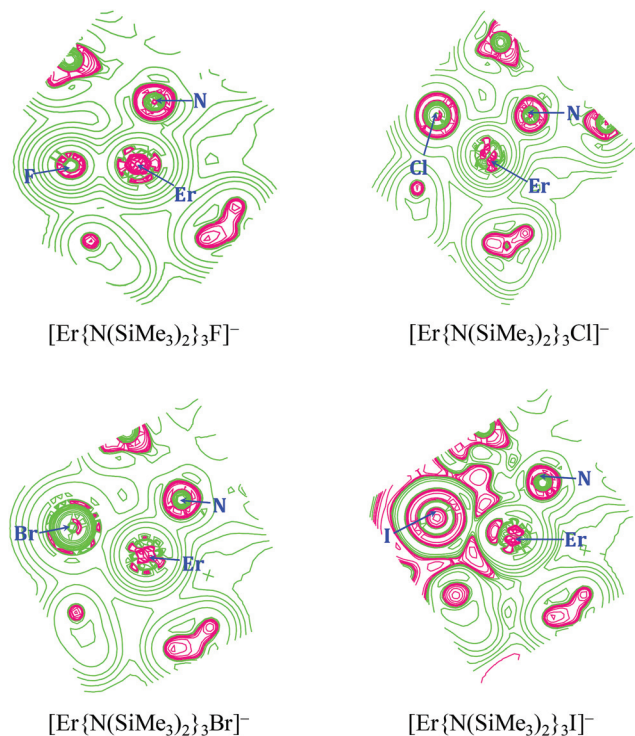
$[Er\{N(SiMe_3)_2\}_3I]^-$

Fig. 9 Contour line diagram of the Laplacian of electron density along the X–Er–N (X = F, Cl, Br, and I) in complex $[Er\{N(SiMe_3)_2\}_3X]^-$ (X = F, Cl, Br, and I). Solid green lines indicate charge depletion $\nabla^2_{\rho(r)} > 0$ and pink line indicated charge concentration $\nabla^2_{\rho(r)} < 0$.

It is evident that the valence shell charge concentration zone of the iodine ligand is more diffused towards the Er(III) ion than other halogens. This indicates that there is a larger charge transfer from I ligand to the Er atom than with other halogens. The small $\rho(r)$, positive $\nabla^2_{\rho(r)}$, and negative $H(r)$ indicate the Er–X covalency increases as we move down to the heavier halogens. Hence, the presence of a heavier halide in the coordination sphere offers a viable way to maximize the gap between the m_J states, irrespective of its position.

To gain further insights into the nature of the interactions present between the Er and ligands, we performed energy decomposition analysis (EDA).[60,83] Here, we have considered two different fragment pairs *viz.* A and B. Fragment pair A investigates the interactions between $Er\{N(SiMe_3)_2\}_3$ and the –Cl ligand, whereas B deals with the interaction between Er–Cl and $(NSiMe)_3$ ligands (see ESI† for further details). The Pauli repulsion is found to be significant for the Er⋯Cl interaction while the presence of $N(SiMe_3)_2$ is found to reduce this repulsion.

The Er⋯Cl electrostatic interaction is estimated to be 214 kcal mol^{-1} while inclusion of $N(SiMe_3)_2$ enhances this value by fivefold (see Table S21 in ESI†). Quite interestingly, –Cl was found to offer a unfavourable steric factor while addition of the $N(SiMe_3)_2$ ligand to the Er(III) more than compensates the steric repulsion energy of the –Cl ligand. EDA analysis affirms the bonding picture described earlier and reveals that this can be utilized to characterize the favourable/

Table 4 CASSCF computed LoProp charges population analysis on Er(III) ion and the atoms in the first coordination sphere of complex **1a**

Atoms	LoProp
Er	2.368
N1	−0.823
N2	−1.265
N3	−1.260
Cl	−1.265
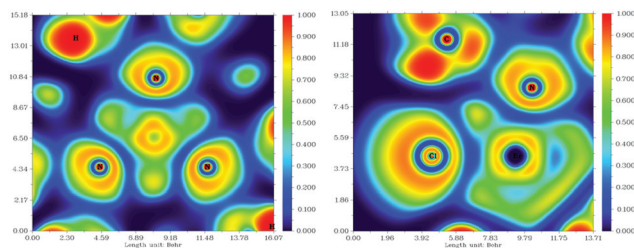
Fig. 10 ELF representation for complex **1a**. The red colour corresponds to a local electron maximum. Left side is the ELF with cut plane of three –N atoms; right side is the ELF with cut plane of Cl–Er–N$_1$.

unfavourable nature of lanthanide–ligand interactions (see Table 4).[29]

Contour maps of ELF[81] for complex **1a** in two different planes are shown in Fig. 10. There is no local maximum between lanthanides and the –N, –Cl donor ligands and therefore the Er–N, Er–Cl bonds are strongly ionic in character. In the valance shell, the local maxima of the ELF are found to be located on the external side of the –N atoms as well as that of the –Cl atoms. Besides strong distortion around Er(III) ion due to asymmetric ligand field is clearly visible in the outer-core shell. Clearly, looking at Fig. 10, the repulsion between the outer core electrons of metal and the valence electrons of the ligands are weaker for the chloride compared to the –N atoms and therefore the core shell is less distorted for in the Er–Cl plane.

Conclusion

Ab initio calculations were performed on a series of $[Er\{N(SiMe_3)_2\}_3Cl]^-$ complexes along with several other model complexes to understand the zero-field SMM characteristic present in this complex. We observed that the zero field SMM characteristic of $[Er\{N(SiMe_3)_2\}_3Cl]^-$ complex is essentially due to various factors such as local symmetry, strength of donor atoms, and geometrical distortions around the Er(III) ion. To understand the role of geometrical distortions, we developed a magneto-structural correlation by changing the out-of-plane shift parameter (τ) and Er–Cl bond distance. The τ parameter is found to be the most significant parameter to fine-tune the U_{cal} values as it brings Er(III) ion in the plane of the equatorial ligand, – an ideal situation for the prolate type ions. The out-

of-plane shift parameter (τ) nicely explains the trend of the barrier height in structurally similar complexes **1–3**. Apart from local geometrical parameters, we also analysed the influence of symmetry on magnetic anisotropy and barrier height. Using continuous symmetry measurement analysis, we developed a correlation/trend between the two high symmetric tetrahedral (**1$_{TD}$**) and trigonal pyramidal (**1$_{TP}$**) structures. Moving from the tetrahedral geometry to trigonal pyramidal geometry *via* a minimal distortion pathway led to a systematic increase in the barrier height. Both the computed and experimental barrier height follow the same trends. All the observed trends and features are well supported by *ab initio* crystal field analysis. Besides, we have also undertaken calculations whereby the Cl ion is substituted by other halogens and found a near linear increase in the barrier height as we move down the halogen group. Our extensive bonding analysis using multiple theoretical tools (AIM, ELF, and EDA analysis) confirm the bonding picture where the Er–X bonds are predominantly electrostatic; however, this picture changes as we move from –F to –I and suggests a viable method to enhance the barrier height by fine-tuning the lanthanide–halogen covalency – a method that differs from other existing approaches.

Conflicts of interest

There are no conflicts to declare.

Acknowledgements

References

1 N. Ishikawa, M. Sugita, T. Ishikawa, S.-y. Koshihara and Y. Kaizu, *J. Am. Chem. Soc.*, 2003, **125**, 8694–8695.

2 D. N. Woodruff, R. E. P. Winpenny and R. A. Layfield, *Chem. Rev.*, 2013, **113**, 5110–5148.

3 J. D. Rinehart and J. R. Long, *Chem. Sci.*, 2011, **2**, 2078–2085.

4 J. D. Rinehart, M. Fang, W. J. Evans and J. R. Long, *Nat. Chem.*, 2011, **3**, 538–542.

5 J. D. Rinehart, M. Fang, W. J. Evans and J. R. Long, *J. Am. Chem. Soc.*, 2011, **133**, 14236–14239.

6 K. R. Meihaus and J. R. Long, *J. Am. Chem. Soc.*, 2013, **135**, 17952–17957.

7 J. L. Liu, J. Y. Wu, Y. C. Chen, V. Mereacre, A. K. Powell, L. Ungur, L. F. Chibotaru, X. M. Chen and M. L. Tong, *Angew. Chem., Int. Ed.*, 2014, **53**, 12966–12970.

8 Y.-C. Chen, J.-L. Liu, L. Ungur, J. Liu, Q.-W. Li, L.-F. Wang, Z.-P. Ni, L. F. Chibotaru, X.-M. Chen and M.-L. Tong, *J. Am. Chem. Soc.*, 2016, **138**, 2829–2837.

9 R. J. Blagg, L. Ungur, F. Tuna, J. Speak, P. Comar, D. Collison, W. Wernsdorfer, E. J. L. McInnes, L. F. Chibotaru and R. E. P. Winpenny, *Nat. Chem.*, 2013, **5**, 673–678.

10 M. N. Leuenberger and D. Loss, *Nature*, 2001, **410**, 789–793.

11 A. Candini, S. Klyatskaya, M. Ruben, W. Wernsdorfer and M. Affronte, *Nano Lett.*, 2011, **11**, 2634–2639.

12 L. Bogani and W. Wernsdorfer, *Nat. Mater.*, 2008, **7**, 179–186.

13 M. Affronte, A. Ghirri, S. Carretta, G. Amoretti, S. Piligkos, G. A. Timco and R. E. P. Winpenny, *Appl. Phys. Lett.*, 2004, **84**, 3468–3470.

14 M. Affronte, *J. Mater. Chem.*, 2009, **19**, 1731–1737.

15 J. Liu, Y.-C. Chen, J.-L. Liu, V. Vieru, L. Ungur, J.-H. Jia, L. F. Chibotaru, Y. Lan, W. Wernsdorfer, S. Gao, X.-M. Chen and M.-L. Tong, *J. Am. Chem. Soc.*, 2016, **138**, 5441–5450.

16 C. R. Ganivet, B. Ballesteros, G. de la Torre, J. M. Clemente-Juan, E. Coronado and T. Torres, *Chem. – Eur. J.*, 2013, **19**, 1457–1465.

17 M. Gregson, N. F. Chilton, A. M. Ariciu, F. Tuna, I. F. Crowe, W. Lewis, A. J. Blake, D. Collison, E. J. L. McInnes, R. E. P. Winpenny and S. T. Liddle, *Chem. Sci.*, 2016, **7**, 155–165.

18 S. K. Gupta, T. Rajeshkumar, G. Rajaraman and R. Murugavel, *Chem. Sci.*, 2016, **7**, 5181–5191.

19 T. Pugh, N. F. Chilton and R. A. Layfield, *Angew. Chem., Int. Ed.*, 2016, **55**, 11082–11085.

20 F.-S. Guo, B. M. Day, Y.-C. Chen, M.-L. Tong, A. Mansikkamäki and R. A. Layfield, *Angew. Chem., Int. Ed.*, 2017, DOI: 10.1002/anie.201705426; C. A. P. Goodwin, F. Ortu, D. Reta, N. F. Chilton and D. P. Mills, *Nature*, 2017, DOI: 10.1038/nature23447.

21 F. Pointillart, O. Cador, B. Le Guennic and L. Ouahab, *Coord. Chem. Rev.*, 2017, **346**, 150–175.

22 C. Görller-Walrand and K. Binnemans, in *Handbook on the Physics and Chemistry of Rare Earths*, ed. K. A. Gschneidner and L. Eyring, Elsevier, Amsterdam, 1996, vol. 23, p. 121.

23 S. Cardona-Serra, J. M. Clemente-Juan, E. Coronado, A. Gaita-Arino, A. Camon, M. Evangelisti, F. Luis, M. J. Martinez-Perez and J. Sese, *J. Am. Chem. Soc.*, 2012, **134**, 14982–14990.

24 P. Zhang, L. Zhang, C. Wang, S. Xue, S.-Y. Lin and J. Tang, *J. Am. Chem. Soc.*, 2014, **136**, 4484–4487.

25 L. Ungur, S. Y. Lin, J. K. Tang and L. F. Chibotaru, *Chem. Soc. Rev.*, 2014, **43**, 6894–6905.

26 J. Tang and P. Zheng, *Lanthanide Single Molecule Magnets*, Springer-Verlag, Berlin, Heidelberg, 2015.

27 J. M. Zadrozny, M. Atanasov, A. M. Bryan, C. Y. Lin, B. D. Rekken, P. P. Power, F. Neese and J. R. Long, *Chem. Sci.*, 2013, **4**, 125–138.

28 J. M. Zadrozny, D. J. Xiao, M. Atanasov, G. J. Long, F. Grandjean, F. Neese and J. R. Long, *Nat. Chem.*, 2013, **5**, 577–581.

29 S. K. Singh, T. Gupta, M. Shanmugam and G. Rajaraman, *Chem. Commun.*, 2014, **50**, 15513–15516.

30 S. K. Singh, T. Gupta and G. Rajaraman, *Inorg. Chem.*, 2014, **53**, 10835–10845.

31 N. F. Chilton, C. A. P. Goodwin, D. P. Mills and R. E. P. Winpenny, *Chem. Commun.*, 2015, **51**, 101–103.

32 N. F. Chilton, *Inorg. Chem.*, 2015, **54**, 2097–2099.

33 M. K. Singh, N. Yadav and G. Rajaraman, *Chem. Commun.*, 2015, **51**, 17732–17735.

34 D. Aravena and E. Ruiz, *Inorg. Chem.*, 2013, **52**, 13770–13778.

35 N. F. Chilton, D. Collison, E. J. McInnes, R. E. Winpenny and A. Soncini, *Nat. Commun.*, 2013, **4**, 2551.

36 S. G. McAdams, A.-M. Ariciu, A. K. Kostopoulos, J. P. S. Walsh and F. Tuna, *Coord. Chem. Rev.*, 2017, **346**, 216–239.

37 S. Gómez-Coca, D. Aravena, R. Morales and E. Ruiz, *Coord. Chem. Rev.*, 2015, **289**, 379–392.

38 J. A. Kitchen, *Coord. Chem. Rev.*, 2017, **340**, 232–246.

39 F. T. Edelmann, *Coord. Chem. Rev.*, 2016, **306**(Part 1), 346–419.

40 P. Martin-Ramos, J. T. Coutinho, M. Ramos Silva, L. C. J. Pereira, F. Lahoz, P. S. P. da Silva, V. Lavin and J. Martin-Gil, *New J. Chem.*, 2015, **39**, 1703–1713.

41 F. Gendron, B. Pritchard, H. Bolvin and J. Autschbach, *Dalton Trans.*, 2015, **44**, 19886–19900.

42 T. Han, Y.-S. Ding, J.-D. Leng, Z. Zheng and Y.-Z. Zheng, *Inorg. Chem.*, 2015, **54**, 4588–4590.

43 A. J. Brown, D. Pinkowicz, M. R. Saber and K. R. Dunbar, *Angew. Chem., Int. Ed.*, 2015, **54**, 5864–5868.

44 F. Aquilante, T. B. Pedersen, V. Veryazov and R. Lindh, *WIREs Comput. Mol. Sci.*, 2013, **3**, 143–149.

45 L. Ungur, M. Thewissen, J. P. Costes, W. Wernsdorfer and L. F. Chibotaru, *Inorg. Chem.*, 2013, **52**, 6328–6337.

46 C. Angeli, R. Cimiraglia and J.-P. Malrieu, *Chem. Phys. Lett.*, 2001, **350**, 297–305.

47 C. Angeli, R. Cimiraglia, S. Evangelisti, T. Leininger and J. P. Malrieu, *J. Chem. Phys.*, 2001, **114**, 10252–10264.

48 F. Neese, *WIREs Comput. Mol. Sci.*, 2012, **2**, 73–78.

49 D. A. Pantazis and F. Neese, *J. Chem. Theor. Comput.*, 2011, **7**, 677–684.

50 B. Metz, H. Stoll and M. Dolg, *J. Chem. Phys.*, 2000, **113**, 2563–2569.

51 K. A. Peterson, D. Figgen, E. Goll, H. Stoll and M. Dolg, *J. Chem. Phys.*, 2003, **119**, 11113–11123.

52 M. J. Frisch, G. W. Trucks, H. B. Schlegel, G. E. Scuseria, M. A. Robb, J. R. Cheeseman, G. Scalmani, V. Barone, B. Mennucci, G. A. Petersson, H. Nakatsuji, M. Caricato, X. Li, H. P. Hratchian, A. F. Izmaylov, J. Bloino, G. Zheng, J. L. Sonnenberg, M. Hada, M. Ehara, K. Toyota, R. Fukuda, J. Hasegawa, M. Ishida, T. Nakajima, Y. Honda, O. Kitao, H. Nakai, T. Vreven, J. A. Montgomery Jr., J. E. Peralta, F. Ogliaro, M. J. Bearpark, J. Heyd, E. N. Brothers, K. N. Kudin, V. N. Staroverov, R. Kobayashi, J. Normand, K. Raghavachari, A. P. Rendell, J. C. Burant, S. S. Iyengar, J. Tomasi, M. Cossi, N. Rega, N. J. Millam, M. Klene, J. E. Knox, J. B. Cross, V. Bakken, C. Adamo, J. Jaramillo, R. Gomperts, R. E. Stratmann, O. Yazyev, A. J. Austin, R. Cammi, C. Pomelli, J. W. Ochterski, R. L. Martin, K. Morokuma, V. G. Zakrzewski, G. A. Voth, P. Salvador, J. J. Dannenberg, S. Dapprich, A. D. Daniels, Ö. Farkas, J. B. Foresman, J. V. Ortiz, J. Cioslowski and D. J. Fox, Gaussian, Inc., Wallingford, CT, USA, 2009.

53 A. D. Becke, *J. Chem. Phys.*, 1993, **98**, 5648–5652.

54 T. R. Cundari and W. J. Stevens, *J. Chem. Phys.*, 1993, **98**, 5555–5565.

55 A. Schafer, C. Huber and R. Ahlrichs, *J. Chem. Phys.*, 1994, **100**, 5829–5835.

56 F. Biegler-König and J. Schönbohm, *J. Comput. Chem.*, 2002, **23**, 1489–1494.

57 T. Lu and F. Chen, *J. Comput. Chem.*, 2012, **33**, 580–592.

58 G. te Velde, F. M. Bickelhaupt, E. J. Baerends, C. Fonseca Guerra, S. J. A. van Gisbergen, J. G. Snijders and T. Ziegler, *J. Comput. Chem.*, 2001, **22**, 931–967.

59 K. Morokuma, *J. Chem. Phys.*, 1971, **55**, 1236–1244.

60 T. Ziegler and A. Rauk, *Theor. Chem. Acc.*, 1977, **46**, 1–10.

61 M. Pinsky and D. Avnir, *Inorg. Chem.*, 1998, **37**, 5575–5582.

62 J. Jung, X. Yi, G. Huang, G. Calvez, C. Daiguebonne, O. Guillou, O. Cador, A. Caneschi, T. Roisnel, B. Le Guennic and K. Bernot, *Dalton Trans.*, 2015, **44**, 18270–18275.

63 L. Ungur and L. F. Chibotaru, *Phys. Chem. Chem. Phys.*, 2011, **13**, 20086–20090.

64 C. Das, A. Upadhyay, S. Vaidya, S. K. Singh, G. Rajaraman and M. Shanmugam, *Chem. Commun.*, 2015, **51**, 6137–6140.

65 J. Jung, F. Le Natur, O. Cador, F. Pointillart, G. Calvez, C. Daiguebonne, O. Guillou, T. Guizouarn, B. Le Guennic and K. Bernot, *Chem. Commun.*, 2014, **50**, 13346–13348.

66 S. K. Singh, T. Gupta, L. Ungur and G. Rajaraman, *Chem. – Eur. J.*, 2015, **21**, 13812–13819.

67 P. Zhang, J. Jung, L. Zhang, J. K. Tang and B. Le Guennic, *Inorg. Chem.*, 2016, **55**, 1905–1911.

68 S. F. Ye and F. Neese, *J. Chem. Theor. Comput.*, 2012, **8**, 2344–2351.

69 H. I. Karunadasa, K. D. Arquero, L. A. Berben and J. R. Long, *Inorg. Chem.*, 2010, **49**, 4738–4740.

70 E. Cremades, S. Gomez-Coca, D. Aravena, S. Alvarez and E. Ruiz, *J. Am. Chem. Soc.*, 2012, **134**, 10532–10542.

71 K. S. Pedersen, G. Lorusso, J. J. Morales, T. Weyhermuller, S. Piligkos, S. K. Singh, D. Larsen, M. Schau-Magnussen, G. Rajaraman, M. Evangelisti and J. Bendix, *Angew. Chem., Int. Ed.*, 2014, **53**, 2394–2397.

72 S. K. Singh, K. S. Pedersen, M. Sigrist, C. A. Thuesen, M. Schau-Magnussen, H. Mutka, S. Piligkos, H. Weihe, G. Rajaraman and J. Bendix, *Chem. Commun.*, 2013, **49**, 5583–5585.

73 S. K. Singh and G. Rajaraman, *Dalton Trans.*, 2013, **42**, 3623–3630.

74 S. K. Singh, N. K. Tibrewal and G. Rajaraman, *Dalton Trans.*, 2011, **40**, 10897–10906.

75 C. Adamo and P. Maldivi, *J. Phys. Chem. A*, 1998, **102**, 6812–6820.

76 D. X. Ma, G. L. Manni and L. Gagliardi, *J. Chem. Phys.*, 2011, **135**, 044128.

77 D. Aravena, M. Atanasov and F. Neese, *Inorg. Chem.*, 2016, **55**, 4457–4469.

78 R. F. W. Bader, *Atoms in Molecules. A Quantum Theory*, Oxford Science Publications, Oxford, 2nd edn, 1990.

79 B. Silvi and A. Savin, *Nature*, 1994, **371**, 683–686.

80 A. D. Becke and K. E. Edgecombe, *J. Chem. Phys.*, 1990, **92**, 5397–5403.

81 L. Joubert, B. Silvi and G. Picard, *Theor. Chem. Acc.*, 2000, **104**, 109–115.

82 J. Narbutt, A. Wodyński and M. Pecul, *Dalton Trans.*, 2015, **44**, 2657–2666.

83 K. Morokuma, *J. Chem. Phys.*, 1971, **55**, 1236–1244.